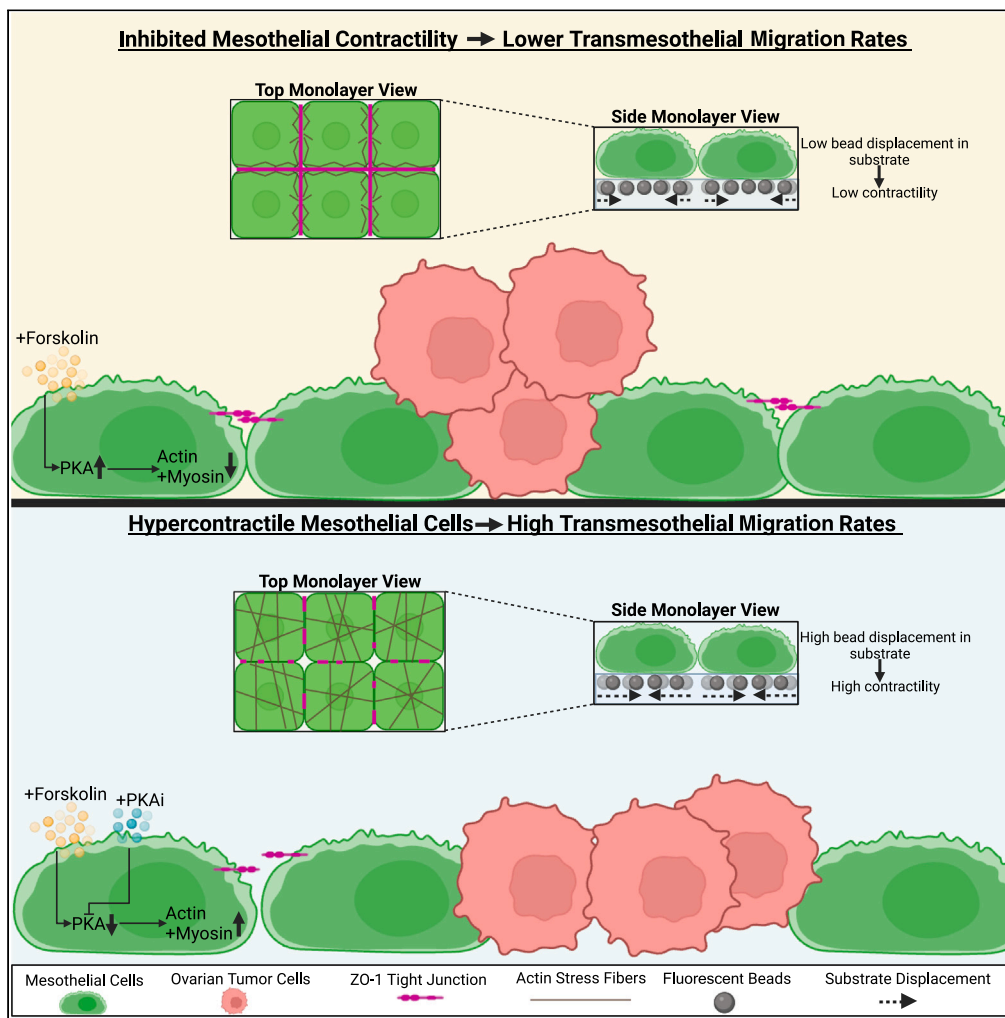


Article

Enhancing PKA-dependent mesothelial barrier integrity reduces ovarian cancer transmesothelial migration via inhibition of contractility



Dorota E. Jazwinska, Youngbin Cho, Ioannis K. Zervantonakis

ioz1@pitt.edu

Highlights

PKA activation in mesothelial cells enhances organization of intercellular junctions

Targeting contractility via ROCK inhibition improves mesothelial barrier function

Mesothelial-targeted approach to limit metastatic potential of solid tumor spheroids

Ovarian cancer cells that form implants exhibit high transmesothelial migration

Jazwinska et al., iScience 27, 109950
June 21, 2024 © 2024 The Author(s). Published by Elsevier Inc.
<https://doi.org/10.1016/j.isci.2024.109950>



Article

Enhancing PKA-dependent mesothelial barrier integrity reduces ovarian cancer transmesothelial migration via inhibition of contractility

Dorota E. Jazwinska,¹ Youngbin Cho,¹ and Ioannis K. Zervantonakis^{1,2,3,4,*}

SUMMARY

Cancer-mesothelial cell interactions are critical for multiple solid tumors to colonize the surface of peritoneal organs. Understanding mechanisms of mesothelial barrier dysfunction that impair its protective function is critical for discovering mesothelial-targeted therapies to combat metastatic spread. Here, we utilized a live cell imaging-based assay to elucidate the dynamics of ovarian cancer spheroid transmesothelial migration and mesothelial-generated mechanical forces. Treatment of mesothelial cells with the adenylyl cyclase agonist forskolin strengthens cell-cell junctions, reduces actomyosin fibers, contractility-driven matrix displacements, and cancer spheroid transmigration in a protein kinase A (PKA)-dependent mechanism. We also show that inhibition of the cytoskeletal regulator Rho-associated kinase in mesothelial cells phenocopies the anti-metastatic effects of forskolin. Conversely, upregulation of contractility in mesothelial cells disrupts cell-cell junctions and increases the clearance rates of ovarian cancer spheroids. Our findings demonstrate the critical role of mesothelial cell contractility and mesothelial barrier integrity in regulating metastatic dissemination within the peritoneal microenvironment.

INTRODUCTION

Most ovarian cancer patients present with metastatic disease that is characterized by tumor growth on the surface of multiple organs in the peritoneal cavity.^{1,2} Following surgical debulking and chemotherapy treatment, the extent of residual tumor implants determines survival outcomes.³ Mesothelial cells form a membrane that lines the surface of peritoneal organs. The integrity of mesothelial cell-cell junctions is critical for the protective barrier function of the peritoneal membrane.⁴ Successful establishment of metastatic tumor implants involves ovarian cancer cell adhesion on mesothelial cells with subsequent invasion and growth that result in organ colonization.⁵ New approaches that dissect the interactions of cancer cells with the mesothelial barrier are urgently needed to identify new targets for blocking metastatic dissemination in ovarian cancer.

The majority of mechanistic studies on ovarian cancer metastasis have taken a cancer cell-centric approach and identified critical cellular programs, including epithelial-to-mesenchymal transition,^{6–8} cell surface receptors^{9–13} and cancer-derived secreted factors.¹⁴ Activation of these programs in cancer cells has been shown to promote pro-metastatic migratory phenotypes via increased cytoskeletal remodeling, contractility,¹⁵ and adhesion to extracellular matrix.^{16,17} In addition to these cancer cell-centric investigations, there is a growing number of studies on the role of mesothelial cells in promoting ovarian cancer metastatic potential. Secretion of extracellular matrix (e.g., fibronectin)^{18,19} by mesothelial cells, as well as paracrine factors (e.g., Wnt5A,²⁰ osteopontin,²¹ CCL2 and IL8)^{22,23} in the metastatic niche have been shown to enhance ovarian cancer aggressiveness. Mesothelial cell transition toward a cancer-associated state has been described to involve secretion of angiopoietin-like 4 and stanniocalcin that in turn promote cancer cell adhesion, migration, and proliferation.²⁴ Furthermore, a proinflammatory environment²⁵ including cytokines enriched in ovarian cancer ascites, such as IL-6²⁶ or cytokines associated with mortality in peritoneal dialysis patients such as IL-1 β ,²⁷ have been shown to induce a mesenchymal state with resultant barrier dysfunction. However, it is currently unknown, whether mesothelial cell-cell junction integrity and cytoskeletal function can be exploited to block ovarian cancer metastatic potential.

We hypothesized that strengthening the mesothelial barrier reduces ovarian cancer metastatic potential, while inducing hypercontractility in mesothelial cells promotes barrier dysfunction and ovarian cancer spheroid transmesothelial migration. We utilized forskolin, an adenylyl cyclase activator, motivated by studies that showed enhanced barrier function in vascular²⁸ and airway epithelial cells treated with forskolin.²⁹ Furthermore, protein kinase A (PKA) a central downstream target of forskolin, has been previously linked with response to inflammatory stimuli³⁰ and regulation of water permeability in mesothelial cells.³¹ However, the role of PKA in regulating cancer-mesothelial interactions during

¹Department of Bioengineering, University of Pittsburgh, Pittsburgh, PA 15261, USA²McGowan Institute for Regenerative Medicine, University of Pittsburgh, Pittsburgh, PA 15219, USA³UPMC Hillman Cancer Center, University of Pittsburgh, Pittsburgh, PA 15232, USA⁴Lead contact

*Correspondence: ioz1@pitt.edu

<https://doi.org/10.1016/j.isci.2024.109950>

transmesothelial migration remains unknown. Here, we evaluated the effects of forskolin on mesothelial clearance for both ovarian and non-ovarian cancer spheroids. We further investigated how perturbing cytoskeletal contractility in mesothelial cells impacts mesothelial cell-cell junction integrity and cancer spheroid clearance *in vitro*. Our study demonstrates a novel approach to modulate mesothelial barrier function and reduce metastatic potential in peritoneal surface malignancies³² independent of cancer genetic background.

RESULTS

In vitro mesothelial barrier clearance in a panel of high-grade serous ovarian cancer models

Ovarian cancer metastatic dissemination involves dynamic interactions of cancer cells with the mesothelial lining. Using an imaging-based assay we monitored ovarian cancer spheroid (tagged with nuclear marker H2B-RFP) migration through a continuous mesothelial monolayer (tagged with GFP) over the course of 24h (Figures 1A and S1A). As early as 4h following ovarian cancer spheroid attachment to the mesothelial monolayer, we observed the formation of mesothelial-free areas (GFP-, shown in white line) that co-localized with ovarian cancer cells (RFP+, shown in yellow line); we termed this as a mesothelial “clearance” event (also described as transmesothelial migration, (Figures 1B and S1B)). We quantified the ratio of the RFP+ surface area occupied by cancer cells to the mesothelial cell-free GFP- areas and found that the clearance efficiency (fraction of ovarian cancer spheroid area that occupied a mesothelial-free surface) increased with time as cancer spheroids interacted with the mesothelial barrier (Figure S1C, see Equation 1 in STAR Methods). We utilized a panel of four human high-grade serous ovarian cancer cell lines (OVCAR8, OVCAR3, OVCA432, OV90) and found that clearance efficiencies exhibited different absolute magnitude 24h following spheroid seeding and temporal rates of change (Figure 1C). These heterogeneous clearance profiles were consistent across two independent mesothelial cell models and primary mesothelial cells (Figures S1D and S1E), with OVCAR8 exhibiting the most aggressive phenotype, followed by OVCA432, OV90 and OVCAR3. Furthermore, we found that neither decreasing (0.3x) nor increasing (3x) cancer spheroid seeding density had any significant impact on the normalized clearance area at 24 h (Figure S1F) and that all ovarian cancer models exhibited similar spheroid sizes (Figure S1G).

To evaluate the physiological relevance of our cancer-mesothelial assay, we next compared spheroid adhesion for OVCAR8 (high-clearance efficiency) and OVCAR3 (low-clearance efficiency) using an *ex vivo* peritoneal wall explant assay.³³ OVCAR8 exhibited a higher fraction of adherent spheroids on the mesothelial monolayer *in vitro* compared to OVCAR3, which was consistent with the *ex vivo* assay results (Figures 1D and 1E). We also compared *in vivo* metastatic outgrowth for OVCAR8 and OVCAR3 using orthotopic xenografts. Using immunostaining for pan-cytokeratin we found that OVCAR8 cancer cells formed invasive tumor implants in multiple peritoneal organs (Figures 1F–1H and S2A–S2C). On the contrary, OVCAR3 cancer cells predominantly localized outside the tissue parenchyma as spheroids (shown also in H&E sections (Figures 1H, S2B, and S2C), while OVCAR8 cells invaded past the mesothelial lining. Quantification of the invasive tumor implant area demonstrated that the high-clearance OVCAR8 model formed larger invasive implants compared to the low-clearance OVCAR3 model (Figure 1G). Collectively, these findings demonstrate that ovarian cancer cells with a capacity to form metastatic implants *in vivo*, also exhibit high clearance rates *in vitro* and adhere strongly on mesothelial barriers *in vitro* and on peritoneal wall explants *ex vivo*.

Forskolin reduces ovarian cancer spheroid transmesothelial migration in a reversible manner that is dependent on protein kinase A

To evaluate whether strengthening the mesothelial barrier alters ovarian cancer spheroid clearance, we utilized the adenylyl cyclase agonist forskolin that has been previously studied in endothelial barriers.³⁴ Mesothelial monolayers were pretreated with forskolin for 72 h prior to addition of ovarian cancer spheroids, while spheroids were formed in the absence of forskolin (Figure 2A). Based on dose-response experiments (Figure S3A) in the high-clearance OVCAR8 cells, we selected a 20 μ M forskolin concentration. We found that forskolin reduced both the absolute magnitude and the temporal rate of normalized clearance for three out of the four ovarian cancer models with baseline clearance efficiency above 20% (Figures 2B and 2C). Specifically, for the OVCAR8 (high-clearance) and OVCA432 (intermediate-clearance) models, there is a 2-fold reduction in clearance efficiency compared to the control, while for OV90 (intermediate-clearance) the forskolin reduction is 1-fold (Figure 2C). Forskolin treatment in OVCAR3 cancer cells (low-clearance) did not significantly change clearance (Figure 2C). To further evaluate how forskolin impacts clearance efficiency, we exposed mesothelial barriers to forskolin for 72h, followed by forskolin removal and seeding of cancer spheroids. Normalized clearance areas and kinetics were similar in the untreated barriers and those where forskolin was removed, suggesting that the presence of forskolin is required to block ovarian cancer clearance (Figure S3B). In addition, we treated mesothelial barriers with forskolin at the same time of seeding ovarian cancer spheroids and found that this was sufficient to reduce ovarian cancer clearance at similar levels compared to 72h forskolin pretreatment (Figure S3C).

We also examined the effects of forskolin on clearance dynamics on mesothelial barriers formed on 3D collagen matrices for the high-clearance OVCAR8 model. We found that forskolin exhibited similar effects on reducing the absolute magnitude and dynamics of normalized clearance area compared to our two-dimensional assay (Figure S3D). To evaluate the relevance of forskolin on limiting mesothelial transmigration across other solid tumors that form peritoneal surface implants,³² we tested a fibrosarcoma (HT1080) and a colorectal adenocarcinoma (CACO-2) cell line. Consistent with the findings in ovarian cancer spheroids, forskolin treatment significantly reduced clearance rates for both fibrosarcoma and colorectal cancer spheroids (Figures S3E and S3F). Finally, we evaluated the effects of forskolin directly on ovarian cancer spheroids. Across all four cancer models, we found that treatment with forskolin had no effect on spheroid spreading area compared to control conditions (Figure S4).

Protein kinase A (PKA) is a central downstream regulator of cellular processes following adenylyl cyclase activation by forskolin.³⁵ As expected, mesothelial cells treated with forskolin exhibited higher levels of PKA activity compared to control (Figure 3A). Next, we used

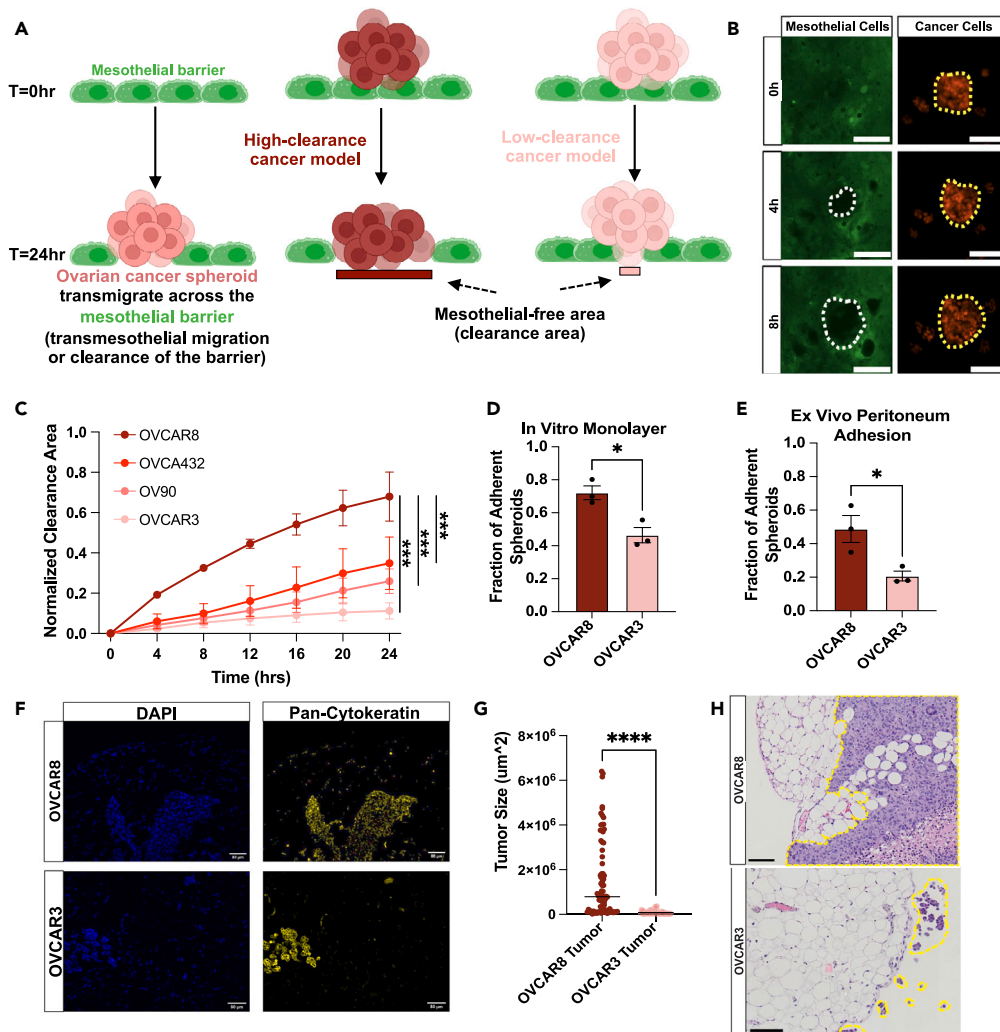


Figure 1. Heterogeneous clearance dynamics in a panel of high-grade serous ovarian cancer models *in vitro* and tumor implant formation efficiency in orthotopic xenografts *in vivo*

(A) Schematic representation of cancer-mesothelial interactions during the process of ovarian cancer spheroid (red) transmigration across a mesothelial monolayer (green). We term this process of transmesothelial migration as clearance of the mesothelial barrier (see Figure S1A for alternative colors in schematic representation).

(B) Representative images of ovarian cancer cells (RFP+) clearing the ZTGFP mesothelial cell monolayer (GFP+) as a function of time. The white line represents the GFP- mesothelial-free area and the yellow line represents the RFP+ cancer spheroid area. Scale bar = 100 μ m.

(C) Normalized clearance area calculated as the ratio of GFP- area (white line in panel B) to the RFP+ cancer area (yellow line in panel B) (see Equation 1 in STAR Methods) in a panel of four ovarian cancer models (OVCAR8, OVCAR3, OVCA432 and OV90) transmigrating across the ZTGFP mesothelial model. Data is mean \pm SEM in $N = 3$ biological replicates. One-way ANOVA *: $p < 0.05$, **: $p < 0.01$, ***: $p < 0.001$.

(D) Quantification of OVCAR8 and OVCAR3 spheroid adhesion to ZTGFP mesothelial monolayers after $T = 3$ h. Data is mean \pm SEM in $N = 3$ biological replicates. T-test *: $p < 0.05$, **: $p < 0.01$, ***: $p < 0.001$, ****: $p < 0.0001$.

(E) Quantification of OVCAR8 and OVCAR3 spheroid adhesion to a murine peritoneal wall after $T = 3$ h. Data is mean \pm SEM in $N = 3$ biological replicates. T-test *: $p < 0.05$.

(F) Representative images of the invasive tumor implants on murine omentum stained for cell nuclei (DAPI) and pan-cytokeratin (yellow) in an orthotopic xenograft. Scale bar = 80 μ m.

(G) Quantification of tumor size in xenografts with OVCAR8 and OVCAR3. Black line = median. $N = 2$ mice with at least $n = 10$ fields analyzed. T-test *: $p < 0.05$, **: $p < 0.01$, ***: $p < 0.001$, ****: $p < 0.0001$.

(H) Representative H&E images of the metastatic tumor implants on omentum. Yellow lines outline tumor cells. Scale bar = 100 μ m.

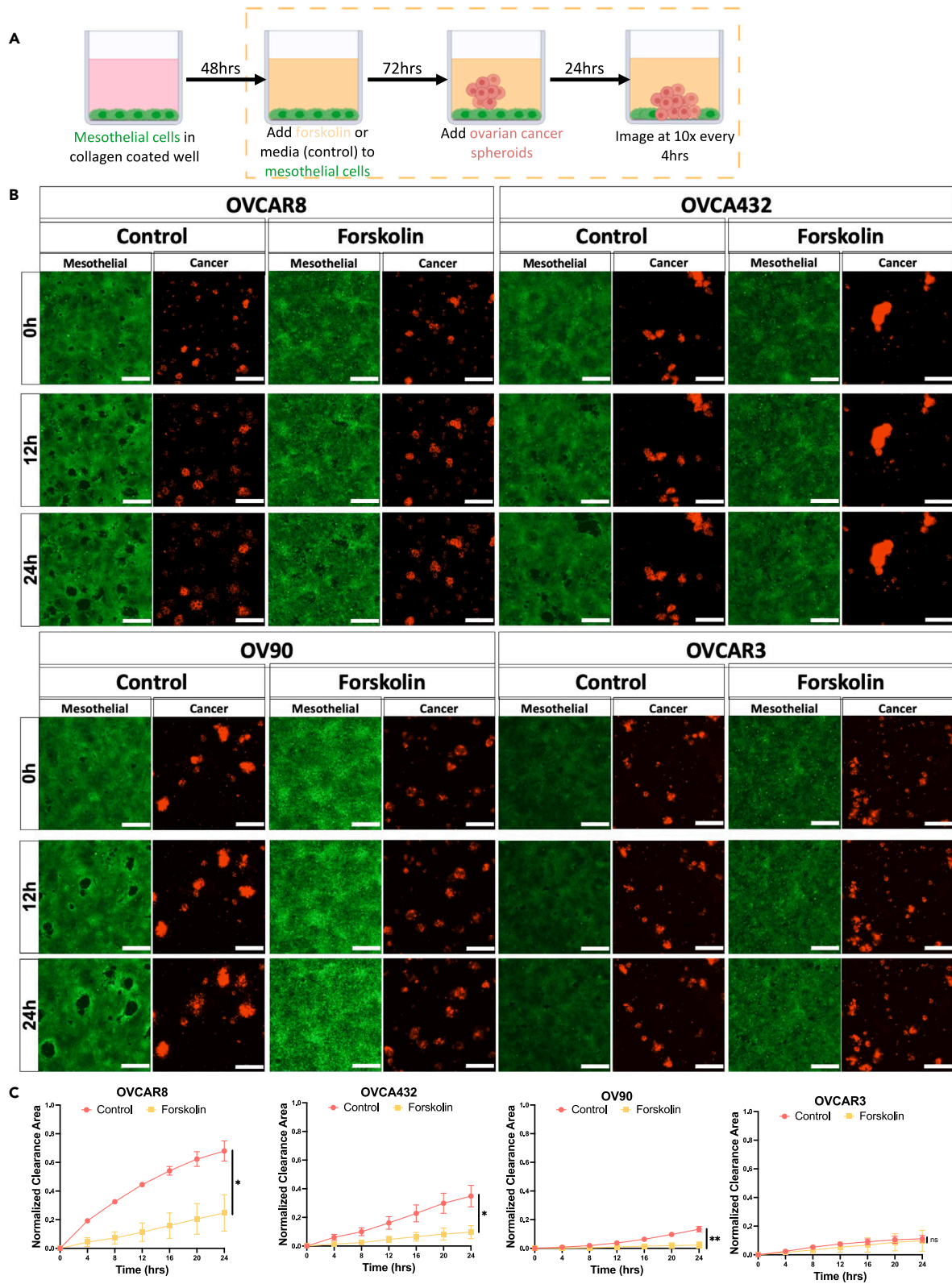


Figure 2. Forskolin reduces clearance efficiency across multiple ovarian cancer spheroids with different baseline clearance rates

(A) Schematic of clearance assay and pre-treatment schedule with forskolin.

(B) Images of mesothelial clearance for control and forskolin pre-treated mesothelial barriers (ZTGFP cells). Green: mesothelial cells; red: ovarian cancer cells. Scale bar = 300 μm .

(C) Analysis of clearance dynamics for control (red) and forskolin-pretreated (20 μM – yellow) ZTGFP mesothelial barriers. Data is mean \pm SEM in $N = 3$ biological replicates. T-test *: $p < 0.05$, **: $p < 0.01$.

PKI-14-22 (PKAi), an irreversible inhibitor of PKA that allowed us to treat only mesothelial cells with PKAi and decouple effects on each cell type. Addition of PKAi in the presence of forskolin reduced phosphorylated PKA levels (Figures 3A and 3B). We found that inhibition of PKA activity in forskolin-treated mesothelial barriers restored clearance rates to control untreated levels (Figures 3C and 3D). This demonstrates the suppressive role of PKA activity in mesothelial clearance. This PKA-dependent effect was more pronounced in cancer models with high baseline clearance efficiency (OVCAR8 and OVCA432). Furthermore, across all four models tested (OVCAR8, OVCA432, OV90, OVCAR3) single agent treatment with PKAi did not alter clearance efficiency compared to the control (Figure 3D). These results were further confirmed by evaluating clearance in mesothelial barriers formed using an independent mesothelial cell line (MeT-5A) and the high-clearance OVCAR8 model (Figure S5A). Taken together, our findings demonstrate that forskolin protects mesothelial barriers from ovarian cancer spheroid transmigration in a PKA-dependent mechanism.

Cell-cell junction organization is enhanced in forskolin-treated mesothelial barriers, with a reduction in actin stress fiber formation and cellular contractility

We next investigated whether the PKA-dependent protective effects of forskolin regulate mesothelial barrier integrity by characterizing the organization and expression of mesothelial cell-cell junctions. Treatment with forskolin promoted the formation of continuous, gap-free adherens (β -catenin) and tight (ZO-1) cell-cell junctions that was reversed upon PKA inhibition (Figure 4A). Single agent inhibition of PKA activity in the absence of forskolin did not impact cell-cell junction organization. Using the length-based metric of “coverage index” we assessed the fraction of cell-cell interface contours that is occupied by junctional protein staining. The coverage index for ZO-1 after forskolin treatment increased by 2-fold compared to the control and reverted to baseline levels when PKA activity was blocked (Figure 4B). Furthermore, we quantified the junction intensity per interface area and found that forskolin induced a 3-fold increase in ZO-1 expression levels compared to the control, whereas combined treatment with forskolin and the PKA inhibitor restored ZO-1 expression back to control levels (Figure 4C). In agreement with the ZO-1 results, β -catenin expression levels increased 1.5-fold after forskolin treatment compared to the control; addition of PKAi restored expression back to control levels in forskolin-treated cells (Figure 4D).

Given the critical role of the cellular cytoskeleton in the maintenance of barrier integrity, we assessed the effects of forskolin and PKA inhibition on actin stress fibers. Consistent with the enhanced organization of cell-cell junctions, forskolin-treated mesothelial cells exhibited weaker formation of stress fibers (25% reduction compared to control) that was restored to control levels in the presence of the PKA inhibitor (Figure 4E). Neutralization of PKA activity in the absence of forskolin did not impact actin stress fiber formation. To investigate whether forskolin affects the stabilization of cell-cell junctions through cytoskeletal remodeling, we evaluated how actomyosin fibers (overlap between phospho-myosin light chain 2 (pMLC2) with actin) interact with ZO-1 tight junctions (Figure 4F). We analyzed the angle between actomyosin fibers and the cell-cell interface (Figure 4G). The forskolin samples showed parallel alignment between ZO-1 junctions at the cell-cell interface and actomyosin fibers. On the contrary, control samples showed perpendicular alignment of actomyosin fibers against weak staining of ZO-1 junctions at the cell-cell interface (Figure 4H). Blockade of PKA activity in forskolin-treated mesothelial cells reverted the stabilization effects of forskolin back to control levels.

To provide a functional assessment of the effects of forskolin on mesothelial cell contractility, we quantified the deformation of a collagen-gel elastic substrate seeded with mesothelial cells. We first investigated the dynamics of bead displacement in the substrate following treatment with forskolin (Figure 5A). Consistent with the clearance results, we found that mesothelial cell-induced bead displacement was suppressed as early as 4 h following addition of forskolin in both single cells (Figure 5B) and in a monolayer (Figure S5B). Next, we evaluated the role of PKA in mesothelial contractility. Substrate displacement fields were not impacted by single agent treatment with the PKA inhibitor, while the PKA inhibitor reverted the forskolin-induced suppression in bead displacement back to the control levels (Figures 5C and 5D). In a set of orthogonal experiments to probe the role of mesothelial cell contractility, we pretreated mesothelial cells using the Rho kinase (ROCK) inhibitor (Y27632). We found that inhibition of ROCK in mesothelial cell monolayers reduced clearance rates and substrate displacements for OVCAR8 spheroids (Figures S6A–S6D). Consistent with the forskolin results, ROCK inhibition in mesothelial cells significantly increased both the coverage index and intensity per interface area of ZO-1 tight junctions (Figures S6B and S6C). These results demonstrate the pro-metastatic effects of cellular contractility, and cell-cell junction organization in the mesothelial barrier via a PKA-dependent mechanism.

Mesothelial cell hypercontractility disrupts cell-cell junctions and promotes ovarian cancer spheroid transmesothelial migration

We next tested how increasing contractility only in mesothelial cells impacts clearance rates in the panel of ovarian cancer models. Mesothelial cells were treated with calyculin A, an inhibitor of myosin II phosphatase that results in hypercontractility (Figures 6A and 6B).³⁶ To confirm mesothelial hypercontractility, collagen-gel elastic substrates were seeded with mesothelial cells. As expected, the substrate displacement fields had higher values when mesothelial cells were treated with calyculin A compared to control conditions (Figure 6C). Temporal analysis of the calyculin

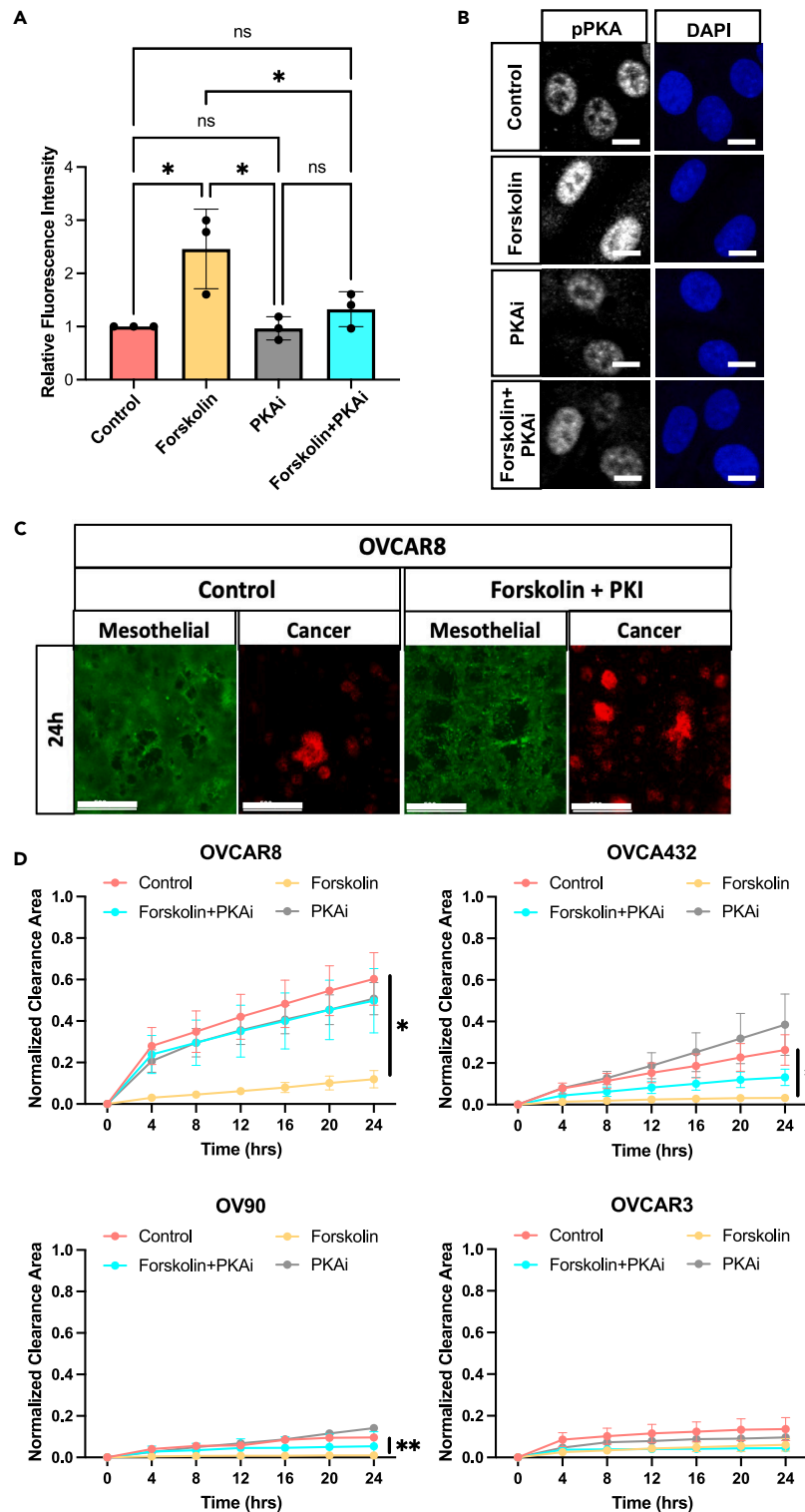


Figure 3. Inhibition of protein kinase A in forskolin-treated mesothelial barriers reverts the protective effects of forskolin across multiple ovarian cancer models

(A) Quantification of phospho-PKA staining of ZTGFP cells in panel B. Data is mean \pm SEM for $N = 3$ biological replicates. One-way ANOVA: *, $p < 0.05$.

(B) Representative images of staining of ZTGFP cells for phospho-PKA (white) and cell nuclei (blue) under the conditions described in panel A. Scale bar = 20 μm .

Figure 3. Continued

(C) Representative images at 24 h of ovarian cancer spheroid (red) and ZTGFP mesothelial barrier (green) for control and combination treatment with forskolin + PKAi (forskolin: 20 μ M; PKA-14-22: 10 μ M). Scale bar = 500 μ m.

(D) Clearance dynamics following treatment with forskolin as a single agent (yellow), PKAi as a single agent (gray), PKAi and forskolin combination (cyan), and control (red) in ZTGFP mesothelial cells. Data is mean \pm SEM in $N = 3$ biological replicates. T-test: * $p < 0.05$, ** $p < 0.01$.

A-treated mesothelial cells revealed continuously increasing displacement levels at a higher rate compared to control conditions (Figure 6D). Next, we monitored the effects of hypercontractile mesothelial barriers on clearance efficiency. Mesothelial cells were pretreated with calyculin A, followed by washout prior to adding cancer cell spheroids. Both the low-clearance OVCAR3 and intermediate-clearance OV90 models exhibited a significant increase in clearance with a 3-fold and 1-fold change respectively (Figure 6B). For the high-clearance OVCAR8 and intermediate-clearance OVCA432 we observed a trend toward higher clearance efficiency that did not reach statistical significance (Figure 6B). We also examined the effects of calyculin A treatment on mesothelial cell-cell junctions and actin stress fibers (Figures 6E–6H). Short-term (30min) after treatment, we found that the hypercontractile mesothelial barriers exhibited a more punctuated and discontinuous staining pattern along the cell-cell boundaries for both adherens (β -Catenin) and tight (ZO-1) cell-cell junctions (Figure 6E). Compared to control conditions, this disrupted junctional organization was characterized by a lower cluster density metric indicating weaker junction protein expression at these fragmented junctions (Figure 6F). Consistent with the reorganized cell-cell junctional patterns, calyculin A-treated mesothelial cells exhibited increased actin stress fiber formation (1.4-fold compared to control; Figures 6G and 6H). In summary, our results suggest that hypercontractile mesothelial cells exhibit impaired monolayer integrity that promotes ovarian cancer spheroid metastatic potential.

DISCUSSION

The mesothelial membrane represents an important line of defense against implantation of ovarian cancer cells, however, the role of mesothelial barrier function in metastatic efficiency remains poorly understood. In this work, we present an imaging-based cancer spheroid-mesothelial interaction assay that enables real-time visualization and quantification of transmesothelial migration (referred to as clearance of the mesothelial barrier). This framework allows us to 1) study how ovarian cancer spheroids clear the mesothelial barrier under control conditions and 2) determine how mesothelial barrier function manipulation can result in altered clearance rates of multiple ovarian cancer cell models. Using both high-grade serous ovarian cancer models and non-ovarian cancer models, we showed that mesothelial cell contractility regulates barrier integrity and can be targeted to reduce clearance rates in a PKA-dependent mechanism.

Our assay is inspired by previous studies that investigated ovarian cancer cell clearance using fluorescently labeled mesothelial monolayers and cancer spheroids. For example, the clearance efficiency of different ovarian cancer models has been linked to mesenchymal reprogramming in cancer cells⁶ and receptor-ligand interactions with mesothelial cells (e.g., ROR2-Wnt5a).³⁷ Using live imaging and tracking of mesothelial cell alignment, a previous study investigated the impact of topological defects in the mesothelial monolayer on ovarian cancer spheroid clearance rates.³⁸ Compared to the non-adherent substrates used for preparing cancer spheroids in the above-mentioned studies, we employed a hanging drop method that resulted in higher cancer spheroid seeding density. Despite this difference, our results showed a higher clearance rate for OVCAR8 compared to OVCAR3 and are consistent with the topological defect study.³⁸ Live-cell imaging assays hold promise for elucidating cancer-mesothelial interactions that promote cancer spheroid adhesion, transmigration, and growth. However, previous studies have not investigated mechanisms regulating mesothelial barrier integrity to develop mesothelial-targeted approaches that limit ovarian cancer clearance.

The mesothelial barrier regulates transport of fluids, proteins and cells in the peritoneal space, and cell-cell junction integrity plays a critical role in these physiological functions.⁴ Our results demonstrate that exposing mesothelial barriers to forskolin, leads to decreased transmesothelial migration (clearance) of both ovarian and non-ovarian (fibrosarcoma and colorectal) cancer spheroids. These results are consistent with transendothelial migration studies, where rates of leukocyte migration decrease when the vascular endothelium is treated with forskolin.³⁹ In addition, forskolin treatment of endothelial barriers rescued the tumor cell-induced hyperpermeability and decreased the transendothelial migration of pancreatic cancer cells.⁴⁰ Forskolin is a widely used inducer of cyclic adenosine monophosphate (cAMP)-driven PKA activation.³⁵ PKA activity in mesothelial cells regulates inflammatory response as evidenced by a previous study that demonstrated PKA-dependent shedding of tumor necrosis factor receptors upon stimulation with interleukin-1 α .³⁰ Furthermore, PKA has been shown to regulate water permeability in rat peritoneal cells with implications in peritoneal dialysis.³¹ In the context of surgery-induced peritoneal injury, delivery of cAMP in a mouse model exhibited a protective effect on the formation of abdominal adhesions.⁴¹ The protective role of cAMP signaling in the peritoneal membrane is also supported by a previous study in rats that demonstrated attenuation of inflammation-induced peritoneal fibrosis by elevating cAMP levels using a phosphodiesterase inhibitor.⁴²

Forskolin also enhanced mesothelial cell-cell junctions by decreasing actin stress fiber formation and contractility in mesothelial cells. This is an important finding because alterations in mesothelial junctions have been linked to aggressive disease in ovarian cancer.⁴³ For example, a previous study showed that compared to benign ascites fluid, cancer-derived ascites fluid downregulated expression of junctional proteins in mesothelial cells and increased the transmigration of the non-serous SKOV3 cancer model through the mesothelial monolayer *in vitro*.⁴⁴ Furthermore, previous immunohistochemical studies in mesothelial cells lining tumor-infiltrated omentum demonstrated reduced staining for cell-cell junctions compared to tumor-free omentum.⁴⁵ Our results also indicate increased transmigration rates when cell-cell junctions are disrupted, as seen when the mesothelial barrier was treated with calyculin A.

In addition to cell-cell junctions, cellular contractility is another important factor that controls mechanical homeostasis of cellular barriers and migratory capacity of individual cells.^{46–48} We found that selective targeting of mesothelial cell contractile function using a ROCK inhibitor

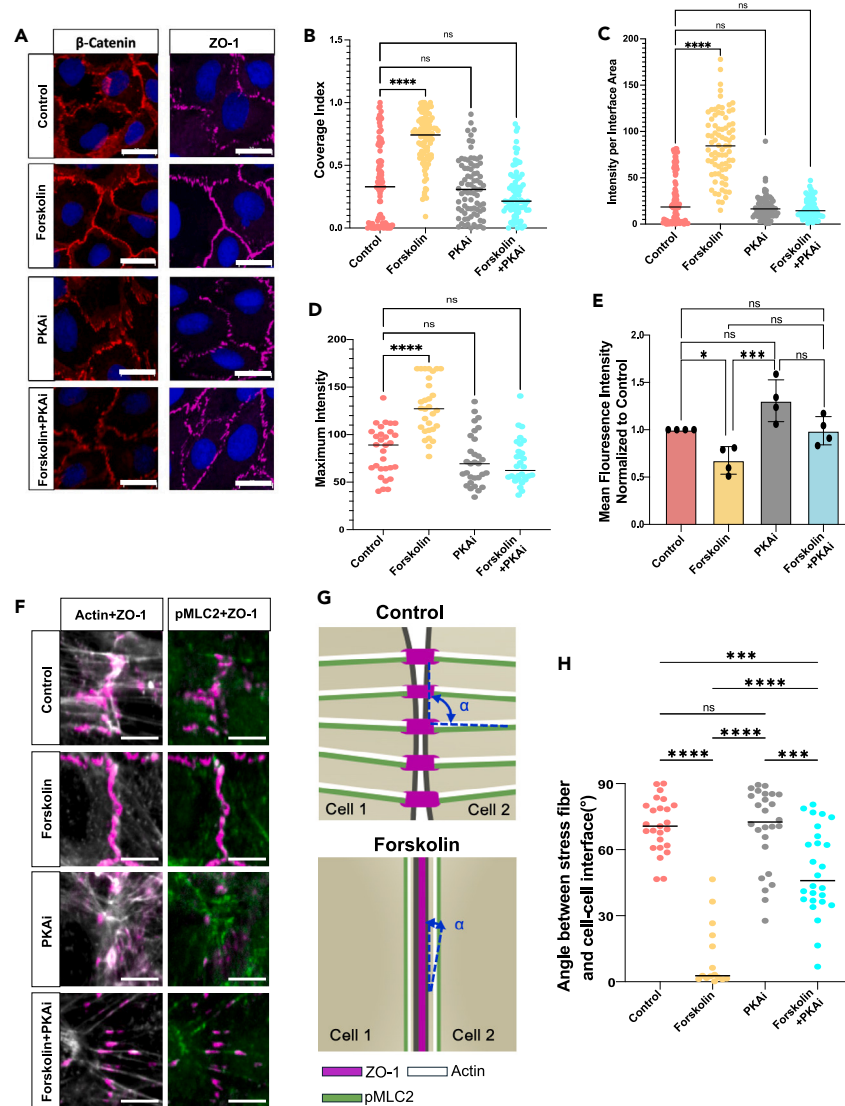


Figure 4. Forskolin enhances mesothelial cell-cell junction integrity and impairs actomyosin fiber formation in a PKA-dependent manner

(A) Staining of cell-cell junctions for β -Catenin (red) and ZO-1 (magenta), cell nuclei (blue) in ZTGFP cells. Scale bar = 20 μ m.

(B) Quantification of coverage index for ZO-1 stained ZTGFP cells. See STAR Methods for Equation 2. Black line = median. $N = 3$ biological replicates. Control $n = 93$, Forskolin $n = 93$, PKAi $n = 80$, and Forskolin+PKAi $n = 77$ junctions. Nonparametric Kruskal-Wallis one-way ANOVA: *: $p < 0.05$, **: $p < 0.01$, ***: $p < 0.001$, ****: $p < 0.0001$.

(C) Quantification of intensity per interface area for ZO-1 stained ZTGFP cells. See STAR Methods for Equation 3. Black line = median. $N = 3$ biological replicates. Control $n = 82$, Forskolin $n = 79$, PKAi $n = 67$, and Forskolin+PKAi $n = 69$ junctions. Nonparametric Kruskal-Wallis one-way ANOVA: *: $p < 0.05$, **: $p < 0.01$, ***: $p < 0.001$, ****: $p < 0.0001$.

(D) Quantification of maximum intensity of β -catenin junctions of ZTGFP mesothelial cells. Black line = median. $N = 3$ biological replicates. $n = 30$ junctions analyzed for all conditions. Nonparametric Kruskal-Wallis one-way ANOVA: *: $p < 0.05$, **: $p < 0.01$, ***: $p < 0.001$, ****: $p < 0.0001$.

(E) Quantification of actin staining intensity of ZTGFP mesothelial cells. Data is mean \pm SEM for $N = 3$ biological replicates; One-way ANOVA: *: $p < 0.05$, **: $p < 0.01$, ***: $p < 0.001$.

(F) Representative images of actin cytoskeleton staining (white), ZO-1 tight junctions (magenta) and phospho-myosin light chain 2 (green) in ZTGFP mesothelial barriers. Scale bar = 10 μ m.

(G) Schematic of analysis methodology for angle between stress fiber and cell-cell interface. ZO-1 (magenta), actin (white) and pMLC2 (green).

(H) Quantification of angle between stress fibers and cell-cell interface. $N = 3$ biological replicates, $n = 5$ junctions per condition. Black line = median. One-way ANOVA: *: $p < 0.05$, **: $p < 0.01$, ***: $p < 0.001$, ****: $p < 0.0001$.

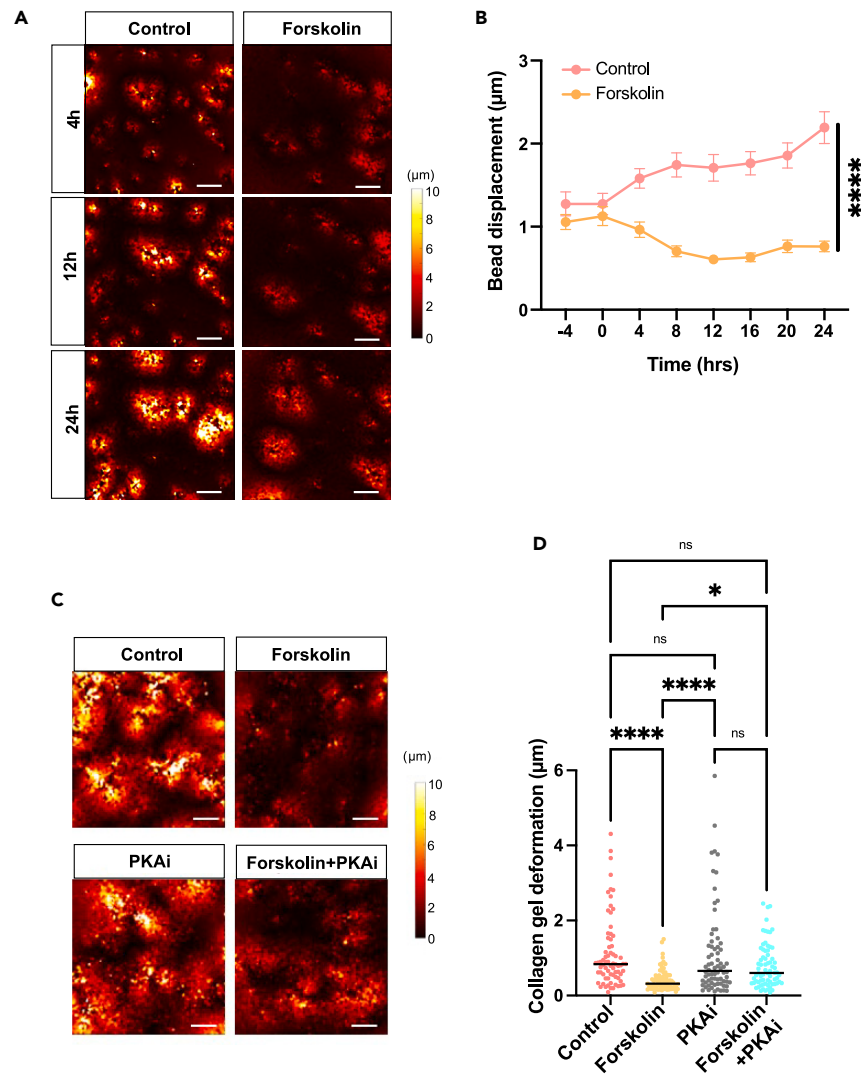


Figure 5. Mesothelial cell contractility is impaired following treatment with forskolin and PKA inhibition restores baseline contractile function

(A) Kinetics of collagen gel substrate displacement fields in control and forskolin-treated (20µM) ZTGFP mesothelial cells. Scale bar = 500µm.
 (B) Quantification of the average bead displacement shown in panel A imaged at 4h intervals. Data is mean ± SEM in n ≥ 37 cells pooled from N = 3 biological replicates. T-test: *p < 0.05, **p < 0.01, ***p < 0.001, ****p < 0.0001.
 (C) Representative displacement fields of collagen substrates seeded with ZTGFP mesothelial cells 24h following treatment with each condition: control (red), forskolin (yellow), PKA inhibitor (gray) and their combination (cyan). Scale bar = 500µm.
 (D) Dot plot of bead displacements by ZTGFP mesothelial cells (n = 195, 252, 108, 246 cells for each condition). N = 3 biological replicates. Black line = median. One-way ANOVA: *p < 0.05, **p < 0.01, ***p < 0.001, ****p < 0.0001.

reduced clearance rates. In ovarian cancer cells, ROCK inhibition has been shown to impact traction forces, mechanosensing and decrease cell motility.⁴⁹ Treatment with forskolin also reduced mesothelial cell contractility and actin stress fibers, thereby enhancing the mesothelial barrier function. This is consistent with previous studies showing that forskolin, in combination with the phosphodiesterase inhibitor rolipram, reduced actin stress fiber formation and enhanced cell-cell junction integrity in endothelial cells exposed to inflammatory stimuli.⁵⁰ These results on forskolin exhibiting a protective effect against transendothelial migration via cytoskeletal remodeling support our findings in ovarian cancer and non-ovarian cancer spheroid clearance. In addition, our results on the fast recovery of mesothelial clearance following forskolin removal are consistent with the reported forskolin kinetics in endothelial barriers.⁵¹

Contrary to forskolin treatment, mesothelial barrier treatment with calyculin A resulted in hypercontractile mesothelial cells, disrupted cell-cell junctions and increased rates of transmesothelial migration. Previous studies in cancer cell monocultures demonstrated that treatment with cancer-derived ascites fluid increases tumor cell contractility as evidenced by increased collagen gel contraction.⁵² In addition to the cancer cell pro-migratory states, the coordinated migratory characteristics of mesothelial cells in a mesothelial monolayer have been shown

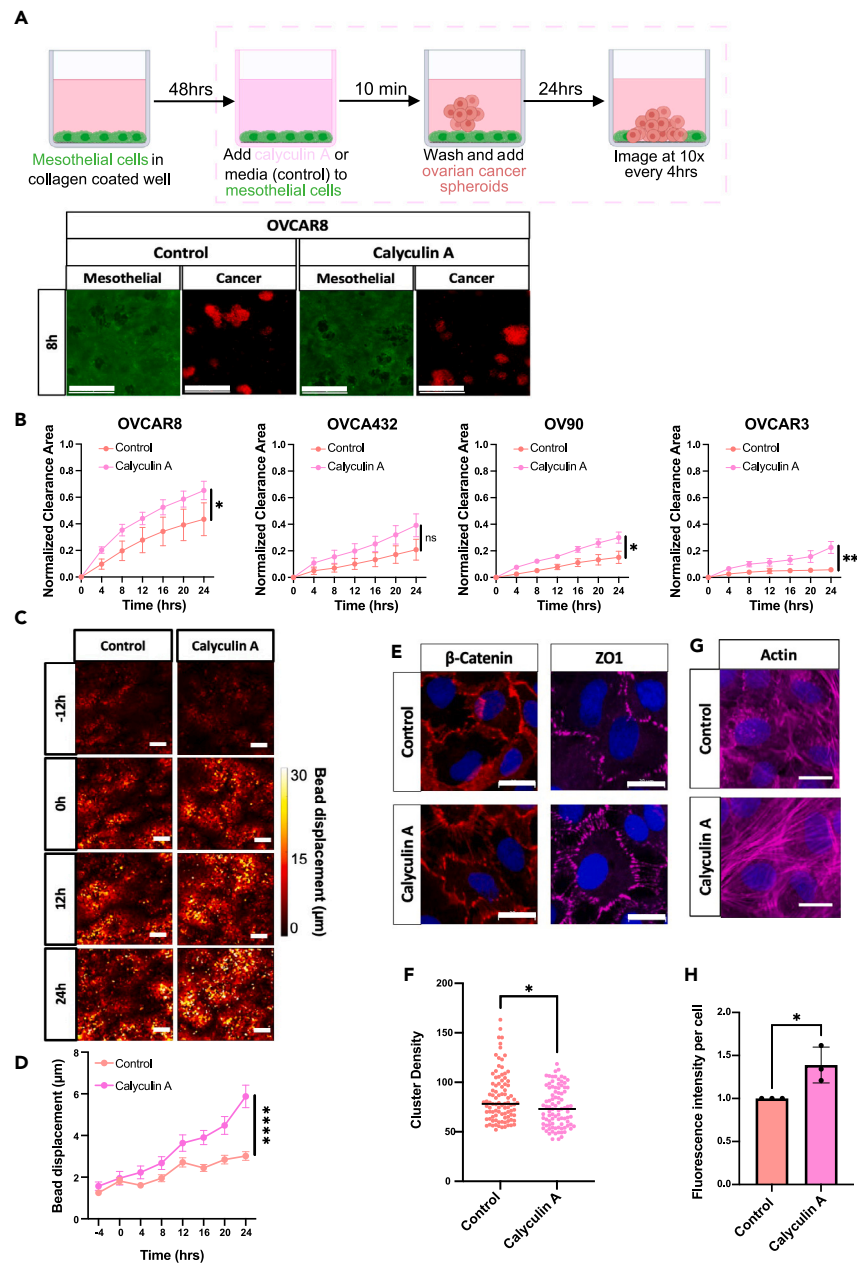


Figure 6. Hypercontractile mesothelial cells exhibit increased clearance efficiency across multiple cancer cell models with impaired cell-cell junction organization and increased actin stress fibers

(A) (Top) Schematic of clearance assay and pre-treatment schedule with calyculin A. (Bottom) Representative images of OVCAR8 spheroids clearing a ZTGF mesothelial barrier treated with calyculin A. Scale bar = 500µm.

(B) Dynamics of normalized clearance areas through ZTGF mesothelial monolayers (green) treated with calyculin A (0.5 nM) for 10 min and washed prior to spheroid addition. Data is mean ± SEM in N = 5 biological replicates. T-test: *: p < 0.05; **: p < 0.01.

(C) Kinetics of collagen gel substrate displacement fields in control and calyculin A-treated ZTGF mesothelial cells. Scale bar = 500µm.

(D) Quantification of ZTGF mesothelial cell-induced collagen substrate displacements following treatment with control (red) and calyculin A (pink). N > 35 cells for each time frame. Data is mean ± SEM in N = 3 biological replicates. T-test: ****: p < 0.0001.

(E) Representative images of ZTGF mesothelial cell-cell junction staining for β-Catenin (red), ZO-1 (magenta) and DAPI cell nuclei (blue). Scale bar = 20µm.

(F) Quantification of ZO-1 staining cluster density. See STAR Methods for Equation 4. Black line = median. N = 3 biological replicates. Control n = 94 and calyculin A n = 90 junctions. Mann-Whitney test: *: p < 0.05; **: p < 0.01.

(G) Representative images of staining for actin cytoskeleton (magenta) and cell nuclei (blue) of ZTGF mesothelial cells. Scale bar = 20µm.

(H) Quantification of actin fluorescence intensity per cell. Data is mean ± SEM in N = 3 biological replicates. T-test *p < 0.05, **p < 0.01.

to create topologic effects that impact ovarian cancer cell clearance *in vitro*.³⁸ Actin cytoskeleton-regulated disassembly of cell-cell junctions has also been shown to play a critical role in the function of non-mesothelial barriers, including epithelial⁵³ and endothelial systems.^{54,55} Our findings on the balance between cell-cell junction organization and cellular contractility are consistent with these previous reports in non-mesothelial barriers and provide new evidence to target hypercontractile mesothelial cells as a possible mechanism to deter ovarian cancer cell metastasis.

We further demonstrated the capability of mesothelial cells to deform the underlying collagen matrix in a PKA-dependent mechanism using relative bead displacement measurements that reflect cellular contractility. Compared to traction force microscopy methods that utilize the force-free state of the matrix and its mechanical properties, our approach does not directly quantify contractile forces.^{56,57} Furthermore, the collagen matrices employed here have been previously shown to exhibit non-elastic properties. These properties can change dynamically as cell-generated forces induce unbinding of matrix bonds, local densification and irreversible deformations in the matrix.^{58–60} In our experiments, the choice of 2 mg/ml for the collagen matrix is informed based on a previous report that characterized collagen type I concentration in cancer-free and cancer-infiltrated omenta.⁶¹ During ovarian cancer progression, matrix composition and architecture have been shown to transition toward a fibrotic state.^{62,63} Previous studies have demonstrated that this dysregulated microenvironment enhances cancer cell sensitivity to growth-factors,⁶¹ invasive phenotypes¹⁶ and mechanosensitivity.⁴⁷ In addition, densification of the extracellular matrix can regulate the mechanical interactions between cells.⁶⁴ Thus, it is critical in future studies to carefully tune matrix composition, mechanical properties, and include additional stromal cell types to design improved 3D models of peritoneal lesions.

Elucidating how mesothelial barrier dysfunction contributes to the establishment of irresectable ovarian cancer implants is critical for discovering new anti-metastatic therapies. Our findings reveal that mesothelial cell-cell junction integrity and contractility represent promising targets to block the metastatic potential of ovarian cancer spheroids; these results have important implications for developing mesothelial-targeted mechanotherapeutic strategies that can be expanded across multiple tumor models with diverse genetic backgrounds. Due to the diversity of the extracellular composition in different peritoneal microenvironments, targeting the dysfunctional mesothelial cell state represents an attractive approach to tackle microenvironment heterogeneity. Finally, our real-time imaging analysis framework that is compatible with multi-well screening technologies provides new opportunities for uncovering therapeutic vulnerabilities during the dynamic cancer-mesothelial interactions in the metastatic cascade and can be employed to the study of other solid tumors that metastasize to the peritoneal cavity.

Limitations of the study

A limitation of this study is the fact that collagen gels utilized for the substrate bead displacement assay can exhibit plastic remodeling, which can influence the measurement of mesothelial cell contractile function. Furthermore, our assessment of ovarian cancer metastatic potential focused on mesothelial-cancer interactions and future studies should investigate other critical microenvironmental factors. Finally, the evaluation of PKA and ROCK-dependent mechanisms was limited to *in vitro* conditions.

STAR★METHODS

Detailed methods are provided in the online version of this paper and include the following:

- KEY RESOURCES TABLE
- RESOURCE AVAILABILITY
 - Lead contact
 - Materials availability
 - Data and code availability
- EXPERIMENTAL MODEL AND STUDY PARTICIPANT DETAILS
 - Cancer cell and mesothelial models
 - *In vivo* mouse experiments
- METHOD DETAILS
 - Mesothelial clearance assay
 - 3D mesothelial clearance assay
 - *Ex vivo* and *In vitro* adhesion assays
 - Live cell imaging and image analysis
 - Collagen gel bead displacement assay
 - Immunofluorescence staining
 - Analysis of mesothelial cell-cell junctions
- QUANTIFICATION AND STATISTICAL ANALYSIS

SUPPLEMENTAL INFORMATION

Supplemental information can be found online at <https://doi.org/10.1016/j.isci.2024.109950>.

ACKNOWLEDGMENTS

This work was supported by the American Cancer Society Research Scholar Grant (RSG-22-168-01-MM to I.K.Z.), US National Institutes of Health (R00 CA222554 to I.K.Z.), the Elsa Pardee Foundation (pilot grant to I.K.Z.), a US National Institutes of Health T32 Fellowship (NIH T32-EB034216, Biomechanics in Regenerative Medicine Training Program to D.E.J.), a National Cancer Center Postdoctoral Fellowship (Y.C.), a Magee Women's Research Institute Ovarian Cancer pilot award, the UPMC Hillman Cancer Center and the Department of Bioengineering, School of Engineering at the University of Pittsburgh. All graphics shown in the paper were created with BioRender.com.

AUTHOR CONTRIBUTIONS

Conceptualization, D.E.J. and I.K.Z.; Methodology, D.E.J., Y.C., and I.K.Z.; Software, D.E.J. and Y.C.; Validation, D.E.J., Y.C., and I.K.Z.; Formal Analysis, D.E.J. and Y.C.; Investigation, D.E.J. and Y.C.; Resources, I.K.Z.; Writing – Original draft, D.E.J., Y.C., and I.K.Z.; Writing – Review and Editing, D.E.J., Y.C., and I.K.Z.; Supervision, I.K.Z.; Funding Acquisition, I.K.Z., Y.C., and D.E.J.

DECLARATION OF INTERESTS

The authors have declared that no competing interest exists.

Received: November 13, 2023

Revised: March 25, 2024

Accepted: May 7, 2024

Published: May 9, 2024

REFERENCES

- Matulonis, U.A., Sood, A.K., Fallowfield, L., Howitt, B.E., Sehouli, J., and Karlan, B.Y. (2016). Ovarian cancer. *Nat. Rev. Dis. Prim.* 2, 16061–16122. <https://doi.org/10.1038/NRDP.2016.61>.
- Bowtell, D.D., Böhm, S., Ahmed, A.A., Aspuria, P.J., Bast, R.C., Beral, V., Berek, J.S., Birrer, M.J., Blagden, S., Bookman, M.A., et al. (2015). Rethinking ovarian cancer II: reducing mortality from high-grade serous ovarian cancer. *Nat. Rev. Cancer* 15, 668–679. <https://doi.org/10.1038/NRC4019>.
- Eisenhauer, E.L., Abu-Rustum, N.R., Sonoda, Y., Aghajanian, C., Barakat, R.R., and Chi, D.S. (2008). The effect of maximal surgical cytoreduction on sensitivity to platinum-taxane chemotherapy and subsequent survival in patients with advanced ovarian cancer. *Gynecol. Oncol.* 108, 276–281. <https://doi.org/10.1016/j.ygyno.2007.10.022>.
- Isaza-Restrepo, A., Martin-Saavedra, J.S., Velez-Leal, J.L., Vargas-Barato, F., and Riveros-Dueñas, R. (2018). The Peritoneum: Beyond the Tissue - A Review. *Front. Physiol.* 9, 738. <https://doi.org/10.3389/fphys.2018.00738>.
- Jazwinska, D.E., Kulawiec, D.G., and Zervantonakis, I.K. (2023). Cancer-mesothelial and cancer-macrophage interactions in the ovarian cancer microenvironment. *Am. J. Physiol. Cell Physiol.* 325, C721–C730. <https://doi.org/10.1152/AJPCELL.00461.2022>.
- Davidowitz, R.A., Selfors, L.M., Iwanicki, M.P., Elias, K.M., Karst, A., Piao, H., Ince, T.A., Drage, M.G., Dering, J., Konecny, G.E., et al. (2014). Mesenchymal gene program-expressing ovarian cancer spheroids exhibit enhanced mesothelial clearance. *J. Clin. Invest.* 124, 2611–2625. <https://doi.org/10.1172/JCI69815>.
- Sawada, K., Mitra, A.K., Radjabi, A.R., Bhaskar, V., Kistner, E.O., Tretiakova, M., Jagadeeswaran, S., Montag, A., Becker, A., Kenny, H.A., et al. (2008). Loss of E-cadherin promotes ovarian cancer metastasis via alpha 5-integrin, which is a therapeutic target. *Cancer Res.* 68, 2329–2339. <https://doi.org/10.1158/0008-5472.CAN-07-5167>.
- Morone, S., Lo-Buono, N., Parrotta, R., Giacomino, A., Nacci, G., Brusco, A., Larionov, A., Ostano, P., Mello-Grand, M., Chiorino, G., et al. (2012). Overexpression of CD157 contributes to epithelial ovarian cancer progression by promoting mesenchymal differentiation. *PLoS One* 7, e43649. <https://doi.org/10.1371/journal.pone.0043649>.
- Huang, Y.L., Liang, C.Y., Ritz, D., Coelho, R., Septiadi, D., Estermann, M., Cumin, C., Rimmer, N., Schötzau, A., Núñez López, M., et al. (2020). Collagen-rich omentum is a premetastatic niche for integrin $\alpha 2$ -mediated peritoneal metastasis. *Elife* 9, 594422–e59534. <https://doi.org/10.7554/ELIFE.59442>.
- Micek, H.M., Rosenstock, L., Ma, Y., Hielsberg, C., Montemorano, L., Gari, M.K., Ponik, S.M., and Kreeger, P.K. (2023). Model of collective detachment in high-grade serous ovarian cancer demonstrates that tumor spheroids produce ECM to support metastatic processes. *APL Bioeng.* 7, 016111. <https://doi.org/10.1063/5.0132254>.
- Iwanicki, M.P., Davidowitz, R.A., Ng, M.R., Besser, A., Muranen, T., Merritt, M., Danuser, G., Ince, T.A., and Brugge, J.S. (2011). Ovarian cancer spheroids use myosin-generated force to clear the mesothelium. *Cancer Discov.* 1, 144–157. <https://doi.org/10.1158/2159-8274.CD-11-0010>.
- Burleson, K.M., Hansen, L.K., and Skubitz, A.P.N. (2004). Ovarian carcinoma spheroids disaggregate on type I collagen and invade live human mesothelial cell monolayers. *Clin. Exp. Metastasis* 21, 685–697. <https://doi.org/10.1007/S10585-004-5768-5>.
- Usui, A., Ko, S.Y., Barengo, N., and Naora, H. (2014). P-cadherin Promotes Ovarian Cancer Dissemination Through Tumor Cell Aggregation and Tumor-peritoneum Interactions. *Mol. Cancer Res.* 12, 504–513. <https://doi.org/10.1158/1541-7786.MCR-13-0489>.
- Bai, S., Ingram, P., Chen, Y.C., Deng, N., Pearson, A., Niknafs, Y.S., O'Hayer, P., Wang, Y., Zhang, Z.Y., Boscolo, E., et al. (2016). EGFL6 Regulates the Asymmetric Division, Maintenance, and Metastasis of ALDH+ Ovarian Cancer Cells. *Cancer Res.* 76, 6396–6409. <https://doi.org/10.1158/0008-5472.CAN-16-0225>.
- Paul, C.D., Mistriotis, P., and Konstantopoulos, K. (2017). Cancer cell motility: lessons from migration in confined spaces. *Nat. Rev. Cancer* 17, 131–140. <https://doi.org/10.1038/NRC.2016.123>.
- Liu, C., Nguyen, R.Y., Pizzurro, G.A., Zhang, X., Gong, X., Martinez, A.R., and Mak, M. (2023). Self-assembly of mesoscale collagen architectures and applications in 3D cell migration. *Acta Biomater.* 155, 167–181. <https://doi.org/10.1016/j.actbio.2022.11.011>.
- Catterall, J.B., Jones, L.M., and Turner, G.A. (1999). Membrane protein glycosylation and CD44 content in the adhesion of human ovarian cancer cells to hyaluronan. *Clin. Exp. Metastasis* 17, 583–591. <https://doi.org/10.1023/A:1006756518500>.
- Ksiazek, K., Mikula-Pietrasik, J., Korybalska, K., Dworacki, G., Jörres, A., and Witowski, J. (2009). Senescent peritoneal mesothelial cells promote ovarian cancer cell adhesion: the role of oxidative stress-induced fibronectin. *Am. J. Pathol.* 174, 1230–1240. <https://doi.org/10.2353/AJPATH.2009.080613>.
- Kenny, H.A., Chiang, C.Y., White, E.A., Schryver, E.M., Habis, M., Romero, I.L., Ladanyi, A., Penicka, C.V., George, J., Matlin, K., et al. (2014). Mesothelial cells promote early ovarian cancer metastasis through fibronectin secretion. *J. Clin. Invest.* 124, 4614–4628. <https://doi.org/10.1172/JCI74778>.
- Asem, M., Young, A.M., Oyama, C., Claire De La Zerda, A., Liu, Y., Yang, J., Hilliard, T.S., Johnson, J., Harper, E.I., Guldner, I., et al. (2020). Host Wnt5a Potentiates Microenvironmental Regulation of Ovarian Cancer Metastasis. *Cancer Res.* 80, 1156–

1170. <https://doi.org/10.1158/0008-5472.CAN-19-1601>.
21. Qian, J., LeSavage, B.L., Hubka, K.M., Ma, C., Natarajan, S., Eggold, J.T., Xiao, Y., Fuh, K.C., Krishnan, V., Enejder, A., et al. (2021). Cancer-associated mesothelial cells promote ovarian cancer chemoresistance through paracrine osteopontin signaling. *J. Clin. Invest.* 131, e146186. <https://doi.org/10.1172/JCI146186>.
 22. Hart, P.C., Kenny, H.A., Grassl, N., Watters, K.M., Litchfield, L.M., Coscia, F., Blaženović, I., Ploetzky, L., Fiehn, O., Mann, M., et al. (2019). Mesothelial Cell HIF1 α Expression Is Metabolically Downregulated by Metformin to Prevent Oncogenic Tumor-Stromal Crosstalk. *Cell Rep.* 29, 4086–4098.e6. <https://doi.org/10.1016/j.celrep.2019.11.079>.
 23. Peng, Y., Kajiyama, H., Yuan, H., Nakamura, K., Yoshihara, M., Yokoi, A., Fujikake, K., Yasui, H., Yoshikawa, N., Suzuki, S., et al. (2019). PAI-1 secreted from metastatic ovarian cancer cells triggers the tumor-promoting role of the mesothelium in a feedback loop to accelerate peritoneal dissemination. *Cancer Lett.* 442, 181–192. <https://doi.org/10.1016/j.canlet.2018.10.027>.
 24. Bajwa, P., Kordylewicz, K., Bilecz, A., Lastra, R.R., Wroblewski, K., Rinkevich, Y., Lengyel, E., and Kenny, H.A. (2023). Cancer-associated mesothelial cell-derived ANGPTL4 and STC1 promote the early steps of ovarian cancer metastasis. *JCI Insight* 8, e163019. <https://doi.org/10.1172/JCI.INSIGHT.163019>.
 25. Jia, D., Nagaoka, Y., Katsumata, M., and Orsulic, S. (2018). Inflammation is a key contributor to ovarian cancer cell seeding. *Sci. Rep.* 8, 12394. <https://doi.org/10.1038/S41598-018-30261-8>.
 26. Shi, Y., Tao, M., Ni, J., Tang, L., Liu, F., Chen, H., Ma, X., Hu, Y., Zhou, X., Qiu, A., et al. (2021). Requirement of Histone Deacetylase 6 for Interleukin-6 Induced Epithelial-Mesenchymal Transition, Proliferation, and Migration of Peritoneal Mesothelial Cells. *Front. Pharmacol.* 12, 722638. <https://doi.org/10.3389/FPHAR.2021.722638>.
 27. Strippoli, R., Benedicto, I., Pérez Lozano, M.L., Cerezo, A., López-Cabrera, M., and Del Pozo, M.A. (2008). Epithelial-to-mesenchymal transition of peritoneal mesothelial cells is regulated by an ERK/NF-kappaB/Snail1 pathway. *Dis. Model. Mech.* 1, 264–274. <https://doi.org/10.1242/DMM.001321>.
 28. Liu, L., Jiang, Y., and Steinle, J.J. (2021). Forskolin regulates retinal endothelial cell permeability through TLR4 actions *in vitro*. *Mol. Cell. Biochem.* 476, 4487–4492. <https://doi.org/10.1007/S11010-021-04252-9>.
 29. Rezaee, F., Harford, T.J., Linfield, D.T., Altawallbeh, G., Midura, R.J., Ivanov, A.I., and Piedimonte, G. (2017). cAMP-Dependent Activation of Protein Kinase A Attenuates Respiratory Syncytial Virus-Induced Human Airway Epithelial Barrier Disruption. <https://doi.org/10.1371/journal.pone.0181876>.
 30. Douvdevani, A., Einbinder, T., Yulzari, R., Rogachov, B., and Chaimovitz, C. (1996). TNF-receptors on human peritoneal mesothelial cells: regulation of receptor levels and shedding by IL-1 alpha and TNF alpha. *Kidney Int.* 50, 219–228. <https://doi.org/10.1038/KI.1996.305>.
 31. Sakurada, T., Kuboshima, S., Ogimoto, G., Fujino, T., Sato, T., Maeba, T., and Kimura, K. (2004). Aquaporin-1 is recruited to the plasma membrane by hyperosmotic stimuli via a protein kinase A-dependent pathway in rat peritoneal mesothelial cells. *Adv. Perit. Dial. Conf.* 20, 37–42.
 32. Cortés-Guiral, D., Hübner, M., Alyami, M., Bhatt, A., Ceelen, W., Glehen, O., Lordick, F., Ramsay, R., Sgarbura, O., Van Der Speeten, K., et al. (2021). Primary and metastatic peritoneal surface malignancies. *Nat. Rev. Dis. Prim.* 7. <https://doi.org/10.1038/S41572-021-00326-6>.
 33. Harper, E.I., and Hilliard, T.S. (2022). In Vivo and Ex Vivo Analysis of Omental Adhesion in Ovarian Cancer. *Methods Mol. Biol.* 2424, 199–216. https://doi.org/10.1007/978-1-0716-1956-8_14.
 34. Fukuhara, S., Sakurai, A., Sano, H., Yamagishi, A., Somekawa, S., Takakura, N., Saito, Y., Kangawa, K., and Mochizuki, N. (2005). Cyclic AMP Potentiates Vascular Endothelial Cadherin-Mediated Cell-Cell Contact To Enhance Endothelial Barrier Function through an Epac-Rap1 Signaling Pathway. *Mol. Cell Biol.* 25, 136–146. <https://doi.org/10.1128/mcb.25.1.136-146.2005>.
 35. Yan, K., Gao, L.N., Cui, Y.L., Zhang, Y., and Zhou, X. (2016). The cyclic AMP signaling pathway: Exploring targets for successful drug discovery (Review). *Mol. Med. Rep.* 13, 3715–3723. <https://doi.org/10.3892/MMR.2016.5005>.
 36. Fabian, L., Troscianczuk, J., and Forer, A. (2007). Calyculin A, an enhancer of myosin, speeds up anaphase chromosome movement. *Cell Chromosome* 6, 1. <https://doi.org/10.1186/1475-9268-6-1>.
 37. Grither, W.R., Baker, B., Morikis, V.A., Ilagan, M.X.G., Fuh, K.C., and Longmore, G.D. (2024). ROR2/Wnt5a signaling regulates directional cell migration and early tumor cell invasion in ovarian cancer. *Mol. Cancer Res.* 22, 495–507. <https://doi.org/10.1158/1541-7786.MCR-23-0616>.
 38. Zhang, J., Yang, N., Kreeger, P.K., and Notbohm, J. (2021). Topological defects in the mesothelium suppress ovarian cancer cell clearance. *APL Bioeng.* 5, 036103. <https://doi.org/10.1063/5.0047523>.
 39. Oppenheimer-Marks, N., Kavanaugh, A.F., and Lipsky, P.E. (1994). Inhibition of the transendothelial migration of human T lymphocytes by prostaglandin E2. *J. Immunol.* 152, 5703–5713.
 40. Hilfenhaus, G., Mompeón, A., Freshman, J., Prajapati, D.P., Hernandez, G., Freitas, V.M., Ma, F., Langenbacher, A.D., Mirkov, S., Song, D., et al. (2021). A High-Content Screen Identifies Drugs That Restrict Tumor Cell Extravasation across the Endothelial Barrier. *Cancer Res.* 81, 619–633. <https://doi.org/10.1158/0008-5472.CAN-19-3911>.
 41. Forman, M.B., Gillespie, D.G., Cheng, D., and Jackson, E.K. (2014). A novel adenosine precursor 2',3'-cyclic adenosine monophosphate inhibits formation of post-surgical adhesions. *Dig. Dis. Sci.* 59, 2118–2125. <https://doi.org/10.1007/S10620-014-3139-X>.
 42. Hung, K.Y., Shyu, R.S., Fang, C.C., Tsai, C.C., Lee, P.H., Tsai, T.J., and Hsieh, B.S. (2001). Dipyridamole inhibits human peritoneal mesothelial cell proliferation *in vitro* and attenuates rat peritoneal fibrosis *in vivo*. *Kidney Int.* 59, 2316–2324. <https://doi.org/10.1046/J.1523-1755.2001.00749.X>.
 43. Zheng, A., Wei, Y., Zhao, Y., Zhang, T., and Ma, X. (2022). The role of cancer-associated mesothelial cells in the progression and therapy of ovarian cancer. *Front. Immunol.* 13, 1013506. <https://doi.org/10.3389/FIMMU.2022.1013506>.
 44. Mikula-Pietrasik, J., Uruski, P., Szubert, S., Szperek, D., Sajdak, S., Tykarski, A., and Książek, K. (2017). Malignant ascites determine the transmesothelial invasion of ovarian cancer cells. *Int. J. Biochem. Cell Biol.* 92, 6–13. <https://doi.org/10.1016/J.BIOCEL.2017.09.002>.
 45. Pakuła, M., Witucka, A., Uruski, P., Radziemski, A., Moszyński, R., Szperek, D., Maksin, K., Woźniak, A., Sajdak, S., Tykarski, A., et al. (2019). Senescence-related deterioration of intercellular junctions in the peritoneal mesothelium promotes the transmesothelial invasion of ovarian cancer cells. *Sci. Rep.* 9. <https://doi.org/10.1038/S41598-019-44123-4>.
 46. Mistriotis, P., Wisniewski, E.O., Bera, K., Keys, J., Li, Y., Tuntithavornwat, S., Law, R.A., Perez-Gonzalez, N.A., Erdogmus, E., Zhang, Y., et al. (2019). Confinement hinders motility by inducing RhoA-mediated nuclear influx, volume expansion, and blebbing. *J. Cell Biol.* 218, 4093–4111. <https://doi.org/10.1083/JCB.201902057>.
 47. Nguyen, R.Y., Cabral, A.T., Rossello-Martinez, A., Zulli, A., Gong, X., Zhang, Q., Yan, J., and Mak, M. (2023). Tunable Mesoscopic Collagen Island Architectures Modulate Stem Cell Behavior. *Adv. Mater.* 35, e2207882. <https://doi.org/10.1002/ADMA.202207882>.
 48. Van Helvert, S., Storm, C., and Friedl, P. (2018). Mechanoreciprocity in cell migration. *Nat. Cell Biol.* 20, 8–20. <https://doi.org/10.1038/S41556-017-0012-0>.
 49. McGrail, D.J., Kieu, Q.M.N., and Dawson, M.R. (2014). The malignancy of metastatic ovarian cancer cells is increased on soft matrices through a mechanosensitive Rho-ROCK pathway. *J. Cell Sci.* 127, 2621–2626. <https://doi.org/10.1242/JCS.144378>.
 50. Waschke, J., Drenckhahn, D., Adamson, R.H., Barth, H., and Curry, F.E. (2004). cAMP protects endothelial barrier functions by preventing Rac-1 inhibition. *Am. J. Physiol. Heart Circ. Physiol.* 287, H2427–H2433. <https://doi.org/10.1152/AJPHEART.00556.2004>.
 51. Klusmeier, N., Schnittler, H.J., and Seebach, J. (2019). A Novel Microscopic Assay Reveals Heterogeneous Regulation of Local Endothelial Barrier Function. *Biophys. J.* 116, 1547–1559. <https://doi.org/10.1016/j.bpj.2019.02.008>.
 52. Sodek, K.L., Murphy, K.J., Brown, T.J., and Ringuette, M.J. (2012). Cell-cell and cell-matrix dynamics in intraperitoneal cancer metastasis. *Cancer Metastasis Rev.* 31, 397–414. <https://doi.org/10.1007/S10555-012-9351-2>.
 53. De Rooij, J., Kerstens, A., Danuser, G., Schwartz, M.A., and Waterman-Storer, C.M. (2005). Integrin-dependent actomyosin contraction regulates epithelial cell scattering. *J. Cell Biol.* 171, 153–164. <https://doi.org/10.1083/JCB.200506152>.
 54. Krishnan, R., Klumpers, D.D., Park, C.Y., Rajendran, K., Trepap, X., Van Bezu, J., Van Hinsbergh, V.W.M., Carman, C.V., Brain, J.D., Fredberg, J.J., et al. (2011). Substrate stiffening promotes endothelial monolayer disruption through enhanced physical forces. *Am. J. Physiol. Cell Physiol.* 300, C146–C154. <https://doi.org/10.1152/AJPCELL.00195.2010>.
 55. Valent, E.T., van Nieuw Amerongen, G.P., van Hinsbergh, V.W.M., and Hordijk, P.L. (2016). Traction force dynamics predict gap formation in activated endothelium. *Exp. Cell Res.* 347, 161–170. <https://doi.org/10.1016/J.YEXCR.2016.07.029>.

56. Zanca, A., Mozetic, P., Orsini, M., Forte, G., and Rainer, A. (2022). A primer to traction force microscopy. *J. Biol. Chem.* **298**, 101867. <https://doi.org/10.1016/J.JBC.2022.101867>.
57. Böhringer, D., Bauer, A., Moravec, I., Bischof, L., Kah, D., Mark, C., Grundy, T.J., Görlach, E., O'Neill, G.M., Budday, S., et al. (2023). Fiber alignment in 3D collagen networks as a biophysical marker for cell contractility. *Matrix Biol.* **124**, 39–48. <https://doi.org/10.1016/J.MATBIO.2023.11.004>.
58. Malandrino, A., Trepap, X., Kamm, R.D., and Mak, M. (2019). Dynamic filopodial forces induce accumulation, damage, and plastic remodeling of 3D extracellular matrices. *PLoS Comput. Biol.* **15**, e1006684. <https://doi.org/10.1371/JOURNAL.PCBI.1006684>.
59. Nam, S., Hu, K.H., Butte, M.J., and Chaudhuri, O. (2016). Strain-enhanced stress relaxation impacts nonlinear elasticity in collagen gels. *Proc. Natl. Acad. Sci. USA* **113**, 5492–5497. <https://doi.org/10.1073/PNAS.1523906113>.
60. Mak, M. (2020). Impact of crosslink heterogeneity on extracellular matrix mechanics and remodeling. *Comput. Struct. Biotechnol. J.* **18**, 3969–3976. <https://doi.org/10.1016/J.CSBJ.2020.11.038>.
61. Fogg, K.C., Renner, C.M., Christian, H., Walker, A., Marty-Santos, L., Khan, A., Olson, W.R., Parent, C., O'Shea, A., Wellik, D.M., et al. (2020). Ovarian Cells Have Increased Proliferation in Response to Heparin-Binding Epidermal Growth Factor as Collagen Density Increases. *Tissue Eng.* **26**, 747–758. <https://doi.org/10.1089/TEN.TEA.2020.0001>.
62. Landry, D.A., Vaishnav, H.T., and Vanderhyden, B.C. (2020). The significance of ovarian fibrosis. *Oncotarget* **11**, 4366–4370. <https://doi.org/10.18632/ONCOTARGET.27822>.
63. Mogi, K., Yoshihara, M., Iyoshi, S., Kitami, K., Uno, K., Tano, S., Koya, Y., Sugiyama, M., Yamakita, Y., Nawa, A., et al. (2021). Ovarian Cancer-Associated Mesothelial Cells: Transdifferentiation to Minions of Cancer and Orchestrate Developing Peritoneal Dissemination. *Cancers* **13**, 1352–1413. <https://doi.org/10.3390/CANCERS13061352>.
64. Nahum, A., Koren, Y., Ergaz, B., Natan, S., Miller, G., Tamir, Y., Goren, S., Kolel, A., Jagadeeshan, S., Elkabets, M., et al. (2023). Inference of long-range cell-cell force transmission from ECM remodeling fluctuations. *Commun. Biol.* **6**, 811. <https://doi.org/10.1038/S42003-023-05179-1>.
65. Mitra, A.K., Davis, D.A., Tomar, S., Roy, L., Gurler, H., Xie, J., Lantvit, D.D., Cardenas, H., Fang, F., Liu, Y., et al. (2015). In vivo tumor growth of high-grade serous ovarian cancer cell lines. *Gynecol. Oncol.* **138**, 372–377. <https://doi.org/10.1016/J.YGYNO.2015.05.040>.
66. Buxboim, A., Rajagopal, K., Brown, A.E.X., and Discher, D.E. (2010). How deeply cells feel: methods for thin gels. *J. Phys. Condens. Matter* **22**, 194116. <https://doi.org/10.1088/0953-8984/22/19/194116>.
67. Mohammadi, H., Arora, P.D., Simmons, C.A., Janmey, P.A., and McCulloch, C.A. (2015). Inelastic behaviour of collagen networks in cell-matrix interactions and mechanosensation. *J. R. Soc. Interface* **12**, 20141074. <https://doi.org/10.1098/RSIF.2014.1074>.
68. Brezovjakova, H., Tomlinson, C., Mohd-Naim, N., Swiatlowska, P., Erasmus, J.C., Huveneers, S., Gorelik, J., Bruche, S., and Braga, V.M. (2019). Junction Mapper is a novel computer vision tool to decipher cell-cell contact phenotypes. *Elife* **8**, e45413. <https://doi.org/10.7554/ELIFE.45413>.

STAR★METHODS

KEY RESOURCES TABLE

REAGENT or RESOURCE	SOURCE	IDENTIFIER
Antibodies		
Rabbit monoclonal anti-ZO-1	Cell Signaling Technology	Cat#8193S
Mouse monoclonal anti-ZO-1	Invitrogen	Cat#33-9100
Mouse anti-β-Catenin Alexa Fluor 647 Conjugated	Cell Signaling Technology	Cat#4627S
Rabbit monoclonal anti-Phospho-PKA Substrate	Cell Signaling Technology	Cat#9624S
Rabbit anti-Phospho-Myosin Light Chain 2 (Ser19)	Cell Signaling Technology	Cat#3671S
Fluorescent Dye 647-I Phalloidin	Abnova	Cat#U0298
Alexa Fluor™ Plus 405 Phalloidin	Invitrogen	Cat#A30104
Goat anti-Rabbit Alexa Fluor 647	Invitrogen	Cat#A32728
Goat anti-Mouse Alexa Fluor 568	Invitrogen	Cat#A11031
Mouse anti-Pan-Cytokeratin eFluor 570	Invitrogen	Cat#41-9003-82
Chemicals, peptides, and recombinant proteins		
Forskolin (from Coleus Forskohlii)	Fisher Scientific	Cat#BP25205
PKI 14-22 amide	Tocris	Cat#2546
Calyculin A	Millipore Sigma	Cat#208851-10UG
Y-27632 2HCl	Selleck Chem	Cat#S1049
CellTracker Green CMFDA dye	Invitrogen	Cat#C7025
CellTracker Red CMPTX dye	Invitrogen	Cat#C34552
Hoechst 33342	Millipore Sigma	Cat#14533-100MG
Experimental models: Cell lines		
OVCAR8	Laboratory of Dr. Joan Brugge, Harvard Medical School	N/A
OVCA432	Laboratory of Dr. Joan Brugge, Harvard Medical School	N/A
OV90	Laboratory of Dr. Joan Brugge, Harvard Medical School	N/A
OVCAR3	Laboratory of Dr. Joan Brugge, Harvard Medical School	N/A
ZTGFP	Laboratory of Dr. Joan Brugge, Harvard Medical School	N/A
MeT-5A	ATCC	CRL-9444
Human Mesothelial Cells	ZenBio	N/A
HT1080	Laboratory of Dr. Roger Kamm, MIT	N/A
CACO-2	Laboratory of Dr. Shikhar Uttam, University of Pittsburgh	N/A
Experimental models: Organisms/strains		
Mouse: C57BL/6	The Jackson Laboratory	RRID:IMSR_JAX:000664
Mouse: NSG	The Jackson Laboratory	RRID:IMSR_JAX:005557
Software and algorithms		
ImageJ	ImageJ	RRID:SCR_003070

(Continued on next page)

Continued

REAGENT or RESOURCE	SOURCE	IDENTIFIER
MATLAB	MathWorks	RRID:SCR_001622
Nikon NIS Elements	Nikon	RRID:SCR_014329
Junction Mapper	Imperial College of London	https://dataman.bioinformatics.ic.ac.uk/junction_mapper/
GraphPad Prism-10	GraphPad	RRID:SCR_002798
RStudio Version 2023.12.1 Build402	Posit Software	RRID:SCR_000432

Other

Collagen Type I, Rat Tail	Corning	Cat#354236
Matrigel Matrix	Corning	Cat#354230
LI-COR Intercept Blocking Buffer	Fisher Scientific	Cat#NC1660556
FluoSpheres™ Carboxylate-Modified Microspheres	Invitrogen	Cat#F8814

RESOURCE AVAILABILITY

Lead contact

Further information and requests for resources and reagents should be directed to and will be fulfilled by the lead contact, Ioannis Zervantonakis, (ioz1@pitt.edu).

Materials availability

This study did not generate new unique reagents.

Data and code availability

- No transcriptomic data were generated in this paper. All microscopy data will be shared by the [lead contact](#) upon request.
- No original code was developed in this paper. Please contact the [lead contact](#) for further information on image analysis procedures using Nikon Elements.
- Any additional information required to reanalyze the data reported in this paper is available from the [lead contact](#) upon request.

EXPERIMENTAL MODEL AND STUDY PARTICIPANT DETAILS

Cancer cell and mesothelial models

All cell lines utilized in this study were cultured in 1:1 ratio of M199 and MCDB 105 media supplemented with 10% heat-inactivated fetal bovine serum (HIFBS) and 5% Penicillin-Streptomycin (GIBCO). ZTGFP human pleural mesothelial cells (gift from Brugge lab, Harvard Medical School), and MeT-5A human pleural mesothelial cells (ATCC) were engineered to express cytoplasmic GFP. Human peritoneal mesothelial cells (ZenBio) were maintained as described by manufacturers' guidelines and stained with CellTracker Green CMFDA dye (10 μ M) prior to live imaging. Ovarian cancer cell lines OVCAR8, OV90, OVCAR3 and OVCA432 (gift from Brugge lab, Harvard Medical School) were engineered to express H2B-RFP. Fibrosarcoma cells, HT1080 (gift from Kamm lab, MIT), and colorectal adenocarcinoma cells, CACO-2 (gift from Uttam lab, UPMC), were dyed with CellTracker Red CMPTX (10 μ M) prior to live imaging. Cell lines were STR authenticated and tested for mycoplasma.

In vivo mouse experiments

Mouse studies were conducted through protocols approved by University of Pittsburgh's Institutional Animal Care and Use Committee (Protocol # 22081542). Female NSG mice (8–10-week-old, Jackson labs) were injected intraperitoneally with 5 million cancer cells. For the OVCAR8 model tissues were harvested 1 month after injection, while for the OVCAR3 model tissues were harvested 2 months after injection. These timepoints were selected due to the differences in *in vivo* tumor growth between the models and are consistent with previous studies.⁶⁵ Solid tumors and abdominal organs (spleen, pancreas, peritoneal wall, ovary) were formalin fixed for immunohistochemical analysis. Tissue sections were prepared and stained with hematoxylin and eosin (H&E). The area of tumor in H&E tissue slides was quantified utilizing ImageJ and at least n>10 fields of view (full image of the peritoneal organs and tumors shown in [Figure S2](#)). For immunofluorescent staining, tissues were deparaffinized, rehydrated and treated with citrate buffer for antigen retrieval in a steamer. Quenching was performed using hydrogen peroxide and treated with Li-Cor Intercept Blocking Buffer. Tissue sections were incubated with pan-cytokeratin (eBioscience 41-9003-82) (1:250) directly conjugated to eFlour 570 overnight and washed with Phosphate Buffer Saline (PBS). Hoechst staining (1hr incubation) was performed to detect nuclei and slides were imaged using a Cytell Cell Imaging System (10X, NA=0.45 objective).

METHOD DETAILS

Mesothelial clearance assay

Mesothelial monolayer formation

Flat bottom 96 well plates (Greiner) were coated with 0.05 mg/mL Rat Tail Collagen Type I (Corning), incubated at 37°C and then washed 3x with PBS prior to cell plating. Mesothelial cells were trypsinized, counted, and plated at 50,000 cells per well in culture medium containing 1% HIFBS. Monolayer formation was verified 48hrs following cell seeding. Forskolin was added at 20 μ M either for 72hrs (pre-treatment) or directly at time of spheroid addition. For the PKA inhibition experiment PKI-14-22 was added 1hr prior to forskolin at a concentration of 10 μ M. For the hypercontractility experiments mesothelial cells were treated with calyculin A (0.5nM) for 10min prior washout. For ROCK inhibitor experiments, Y27632 (5 μ M) was added to the mesothelial monolayers for 1hr prior to washout and spheroid addition.

Ovarian cancer spheroid formation

Ovarian cancer cells were trypsinized, counted and resuspended at a density of 200,000 cells/mL with 2% v/v matrigel in 10% HIFBS culture media. Spheroids were generated by dispensing 5 μ l droplets on the top lids of 10cm tissue culture dishes and 5mL of PBS was added to the dish once inverted to keep the spheroids from drying out. Cancer cells were incubated for 72hrs allowing the spheroids to form. The spheroids were resuspended in 1% HIFBS media (1 plate of spheroids resuspended in 500 μ l) and 50 μ l was added per well into mesothelial monolayers treated as described above. For experiments utilizing varying spheroid densities the spheroids were either resuspended at regular density, 3-fold diluted (0.3x) or concentrated (3x) prior to seeding on the monolayers. Plates were spun at 900 RPM for 1 minute to promote spheroid settling at the bottom of the plate.

3D mesothelial clearance assay

We formed 3D collagen type I hydrogels (2mg/ml) on the bottom of each well in a flat bottom 96 well-plate (Greiner). Mesothelial cells were trypsinized, counted, and plated at 50,000 cells per well in culture medium contain 1% HIFBS. Monolayer formation was verified 48hrs following cell seeding. Forskolin was added at 20 μ M for 72hrs and spheroids were added utilizing the [STAR Methods](#) described above. Analysis was done as described below.

Ex vivo and In vitro adhesion assays

Ex vivo adhesion assay

To examine spheroid adhesion in a physiologically-relevant platform, we adapted a previous protocol.³³ Female C57BL/6 mice (8-10-week-old, Jackson labs) were sacrificed, and the peritoneal wall was removed. Tissue explants were punched using 6mm biopsy punch and placed on double sided tape with the interior surface of the peritoneal wall facing up. Polydimethylsiloxane (PDMS) was prepared at a 10:1 (w/w) base:curing agent ratio, mixed and baked at 80C overnight. PDMS devices were punched with a 4mm biopsy punch and bonded on top of the tissue to secure it in place prior to loading spheroids. Ovarian cancer spheroids (OVCAR8 and OVCAR3) were made using the hanging drop method described above. The spheroids were resuspended in medium and 20 μ l was added per device. The spheroids were left to adhere for 3hrs at 37°C and pre-wash images were taken using a confocal microscope (ZEISS LSM700). Then the devices were washed 3x with 200 μ l of PBS to remove any nonadherent spheroids and imaged to determine the fraction of spheroids that adhered. We utilized intensity thresholding in the Nikon NIS Elements software to quantify the total area of spheroids prior to and after washing. To obtain the fraction of adherent spheroids, the area of spheroids after the wash was divided by the total area of spheroids before washing.

In vitro adhesion assay

Flat bottom 96 well plates (Greiner) were coated with 0.05 mg/mL Rat Tail Collagen Type I (Corning), incubated at 37°C and then washed 3x with PBS prior to cell seeding. Mesothelial cells were trypsinized, counted, and plated at 50,000 cells per well in culture medium contain 1% HIFBS. Monolayer formation was verified 48hrs following cell seeding. Ovarian cancer spheroids (OVCAR8 and OVCAR3) were made using a hanging drop method. The spheroids were resuspended in starvation media and 100 μ l was added per well. The spheroids were left to adhere for 3hrs at 37°C and imaged pre-wash utilizing the Cytation5-BioSpa8 Imaging system. Then the plate was washed 3x with 200 μ l of PBS to remove any nonadherent spheroids. Image analysis and quantification was performed using the same method described for the *ex vivo* assay above.

Live cell imaging and image analysis

Imaging was performed utilizing the Cytation5-BioSpa8 Imaging system. Laser autofocus was utilized and the images were captured using a 10x/NA=0.3 objective every 4 hours. The images for analysis included 6 fields of view stitched with a 10% overlap. Spheroid and clearance area quantifications were performed using Nikon NIS Elements software. Using intensity thresholds, we detected GFP- (GFP-negative in [Equation 1](#) below) mesothelial-free surfaces and RFP+ spheroid that were used to define two separate masks. By using binary operators on these masks, we identified GFP- areas that had direct overlap with a RFP+ spheroid to determine clearance events. Both the clearance areas and RFP+ spheroids were tracked as objects in NIS Elements software. Both GFP- and RFP+ mask outputs were imported as CSV files into RStudio. Normalized clearance area was calculated by reporting a baseline subtracted (to account for differences in initial plate imaging step at time zero) GFP- area and then divided by the spheroid area at time zero.

$$\text{Normalized Clearance Area} \left(t \right) = \frac{\text{GFP negative area} (t) - \text{GFP negative area} (t = 0\text{hrs})}{\text{Spheroid area} (T = 0\text{hrs})} \quad (\text{Equation 1})$$

Collagen gel bead displacement assay

Fluorescence beads (diameter 1.0 μm) were mixed in a 2 mg/ml collagen type I gel and added at 24 μl per well in 12 well-glass bottom plates. Following coverglass (diameter 18mm) placement on top of the collagen gel solution these plates were incubated upside down in 4°C for 10 minutes. Next, plates were transferred to 37°C and incubated for an additional 40 minutes. These 50 minutes of incubation allowed for collagen gel polarization and subsequently 1ml PBS was added to each well and the coverglass was removed using a razor blade. ZT mesothelial cells were plated at 10,000 cells per well for individual cell analysis and 350,000 cells per well for the monolayer analysis and allowed to attach for three hours before imaging. Cells were treated with calyculin A (0.5nM) for 10 minutes and washed with culture medium prior to imaging, PKI-14-22 (10 μM) was added one hour prior to forskolin (20 μM) or forskolin (20 μM) alone was added right before imaging step. In the experiments using ROCK inhibitor, mesothelial cells were treated with Y27632 (5 μM) for 1hr following washout. The maximum duration of these experiments was 48hrs, where the collagen gel remained attached to the well-plate (no coating was applied). Furthermore, the thickness of our collagen matrices was \sim 100 μm , which is 20-fold larger than gel thickness values shown previously to impacted by a rigid substrate.⁶⁶ Bead displacement was analyzed using a custom MATLAB script and plotted using GraphPad Prism. Reference bead images were acquired immediately after seeding the cells on the collagen gel (initial bead positions as described in a previous report).⁶⁷ We then monitored the same imaging field over time and calculated relative displacements to the initial bead positions.

Immunofluorescence staining

Cells were fixed with 4% paraformaldehyde (PFA) for 15 minutes at room temperature and three PBS washes, followed by permeabilization with 0.1% Triton X-100 for 10 minutes at room temperature and washed three times with PBS. The plates were blocked for 1 hour with Intercept Blocking Buffer. Primary antibodies against ZO-1 (Cell Signaling Technology, 8193) (1:250), ZO-1 (Invitrogen, 33-9100) (1:50), β -Catenin (Cell Signaling Technology, 4627) (1:250), Phospho-PKA Substrate (Cell Signaling Technology, 9624) (1:250), Phospho-Myosin Light Chain 2 (Ser19) (Cell Signaling Technology, 3671) (1:50), Alexa 647 Phalloidin (Abnova, U0298) (1:1000) and Alexa 405 Phalloidin (Invitrogen, A30104)(1:1000) were incubated overnight at 4°C in the dark. After washing the primary antibodies three times with PBS, Alexa 647 or Alexa 568 secondary antibodies (1:500) and Hoechst (1:1000) were added to the samples and incubated for 1 hour at room temperature in the dark. Plates were imaged using fluorescent confocal microscopy (Zeiss LSM700). Image analysis was done using ImageJ.

Analysis of mesothelial cell-cell junctions

Junction Mapper⁶⁸ was utilized to evaluate junction staining (please see original methods⁴⁷ for details on metrics and schematics). Briefly, cell boundaries were automatically identified using ZO-1 followed by manual annotation of junction corners. We measured the interface contour and area, the fragmented junction contour and area, as well as the intensity for ZO-1. The equations employed to quantify these parameters are described below:

$$\text{a) Coverage Index} = \frac{\text{fragmented junction contour}}{\text{interface contour}} * 100\% \quad (\text{Equation 2})$$

$$\text{b) Cluster Density} = \frac{\text{junction protein intensity}}{\text{fragmented junction area}} * 100\% \quad (\text{Equation 3})$$

$$\text{c) Intensity per Interface Area} = \frac{\text{junction protein intensity}}{\text{interface area}} \quad (\text{Equation 4})$$

β -catenin expression was quantified utilizing ImageJ to acquire line profiles of 10 cells per replicate and determine the maximum intensity for each junction.

To analyze the organization of contractile fibers with respect to the cell-cell interface, we employed ImageJ and manually outlined ZO-1 junctions and actomyosin fibers defined by colocalization of phospho-myosin light chain 2 with actin. Subsequently, we calculated the angle between the actomyosin fibers and cell-cell interface as shown in Figure 4G. We analyzed a minimum of 3 actin fibers for each junction and 5 junctions per condition.

QUANTIFICATION AND STATISTICAL ANALYSIS

Values are reported as mean +/- standard error of the mean (SEM) unless stated otherwise. We calculated the mean values of at least three biological experiments, with each having at least three technical replicates. Significance was assessed using t-tests (two-sample) or one-way ANOVA (multiple comparisons) in GraphPad Prism (v 10). When the underlying distributions were not normal significance was assessed using Mann-Whitney test (two-sample) or one-way nonparametric Kruskal-Wallis ANOVA (multiple comparisons) in GraphPad Prism (v10). P values below 0.05 were considered significant and the level of significance (*p<0.05, **p<0.01, ***p<0.001, ****p<0.0001) was labeled utilizing asterisks in the figures.